

# Low-Dimensional Dynamics and Modeling of Shock-Separation Interaction over Turrets at Transonic Speeds

Alexander Vorobiev<sup>1</sup>, Stanislav Gordeyev<sup>2</sup>, Eric Jumper<sup>3</sup>  
*University of Notre Dame, Notre Dame, Indiana, 46545*

Sivaram Gogineni<sup>4</sup>,  
*Spectral Energies, LLC, Dayton, OH 45431*

Alexis Marruffo<sup>5</sup> and Donald J. Wittich<sup>6</sup>  
*Air Force Research Laboratory, Directed Energy Directorate, Kirtland AFB, NM 87117*

**Extensive studies of the local shock dynamics in transonic compressible flow near partially-protruding cylindrical turret are presented and discussed. Spatially-temporally resolved wavefront measurements with a high-speed Shack-Hartmann sensor, synchronized with high-speed shadowgraph system and unsteady pressure measurements on the turret surface were performed for a range of incoming transonic Mach numbers. It was found that the pressure field, the shock and the separation region exhibit almost periodic strong oscillations, with its frequency inversely proportional to the low speed. Based on the unsteady pressure near the shock, the phase-locked averaging technique was employed to reveal phase-averaged details of the shock and the separation region dynamics. The low-dimensional model, based on time-delayed feedback, is proposed and was shown to properly predict essential features of the shock-separation interaction. Relevance of the proposed feedback mechanism for transonic flows around realistic turrets is discussed.**

## I. Introduction

For many practical applications which require sending or transmitting a laser beam from an airborne platform, turrets provide convenient means to point-and-steer the laser beam. However, a turret creates a complex turbulent flow around it [1] with significant turbulence-related distortions imposed on an outgoing laser beam, so-called aero-optical distortions [2,3], even at relatively low subsonic speeds [1]. These aero-optical effects result in unwanted unsteady beam defocus and jitter on the target, disrupting a high-speed optical link in free-space laser-based communication systems, for instance.

When the flow is subsonic everywhere around the turret, essential flow features and related aero-optical distortions have been extensively studied in last few years and are believed to be fairly well-understood [1,3-7]. But for incoming Mach numbers larger than approximately 0.55, the flow on top of the turret becomes locally supersonic, with a resulting local unsteady shock [1,5]. The shock creates additional unsteady density gradients in the flow and creates a larger separation region downstream of the turret, as the shock promotes an earlier separation of the flow off the turret. All these shock-related features add additional time-dependent aero-optical distortions to the outgoing beam [5, 8].

Despite an extensive research in a shock-boundary-layer interaction for the last fifty years, primarily related to transonic flows over airfoils [9-15], several key aspects of this interaction are still not well understood. The case of a stronger interaction between the shock and the separated region over bodies with a large streamwise curvature, like

---

<sup>1</sup> Post-Doctoral Assistant, Department of Mechanical and Aerospace Engineering, Hessert Laboratory for Aerospace Research, Notre Dame, IN 46556, AIAA Member.

<sup>2</sup> Research Associate Professor, Department of Mechanical and Aerospace Engineering, Hessert Laboratory for Aerospace Research, Notre Dame, IN 46556, AIAA Associate Fellow.

<sup>3</sup> Professor, Department of Mechanical and Aerospace Engineering, Hessert Laboratory for Aerospace Research, Notre Dame, IN 46556, AIAA Fellow.

<sup>4</sup> President, 5100 Springfield St. Suite 301, Dayton OH 45431, Senior AIAA Member.

<sup>5</sup> Aero-Optics Engineer, Laser Division, 3550 Aberdeen Ave SE.

<sup>6</sup> Aerospace Engineer, Laser Division, 3550 Aberdeen Ave SE.



The turret has a rectangular optical assembly with a square aperture 30mm x 30mm, with its outer cylindrical lens having the same curvature as the turret surface, see Figure 1, right; the assembly also has a matching negative-focal-length cylindrical lens and a return mirror, so the whole assembly works as an optical flat. The test section was equipped with 9 static pressure ports, marked by P1..P9 in Figure 1, left, located at the side wall of the test section to monitor static pressure distribution along the test section. Two unsteady pressure ports K10 and K11 in Figure 1, left, were fitted with Kulite pressure transducers for time-resolved measurements of the flow downstream of the turret. Additional nine Kulite unsteady pressure sensors, K1..K9, were placed in a staggered manner adjacent to the optical aperture, with the angular step of 3.67 degrees spanning from -14.67 degrees to 14.67 degrees from the middle of the aperture, see Figure 1, right. Locations on the turret surface are characterized by an elevation angle,  $\theta$ , shown in Figure 1, left; the elevation angle of zero corresponds to the upstream direction and positive values are in the clockwise direction.

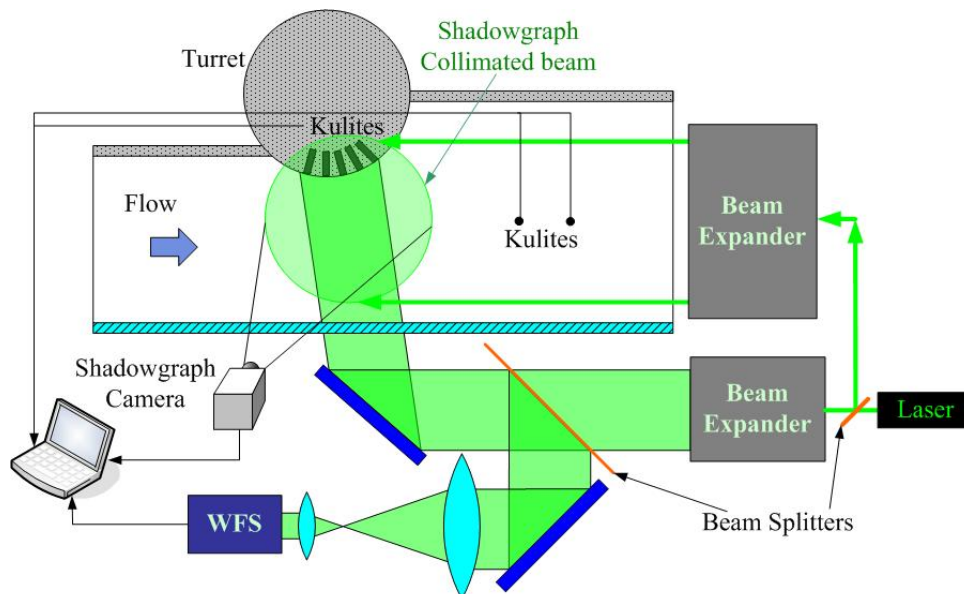
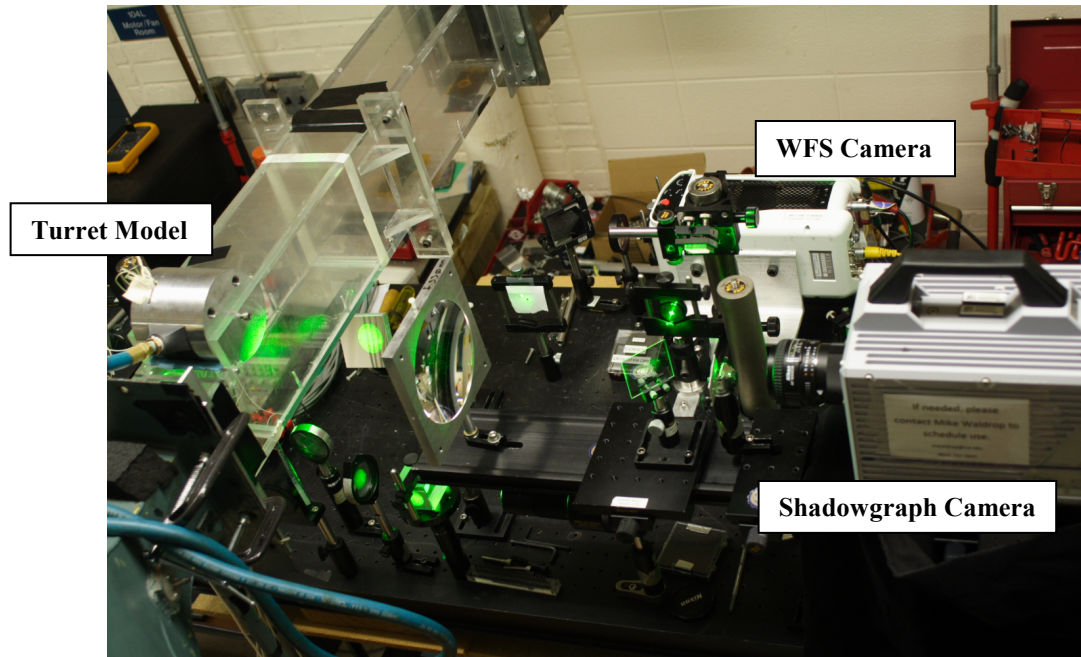


Figure 2. Picture (top) and schematics (bottom) of the time-resolved Shadowgraph/Wavefront/Pressure set-up.

For time-resolved wavefront measurements, the collimated Nd:YAG laser beam 40 mm in diameter was transmitted into the test section using steering mirrors. The beam was directed into the optical assembly inside the cylinder and reflected back along the same path, thus using a double-path approach and increasing the signal by factor of two. The returning beam was split aside and directed to a high-speed Shack-Hartmann wavefront sensor, see Figure 2 for picture and schematic of the optical set-up. The sensor measured aero-optical distortions over a portion of the aperture area 30 mm x 15 mm with the spatial resolution of 60x30 subapertures, with 60 subapertures in the streamwise direction; the wavefront sensor sampling rate was 13.5 kHz. Aero-optical measurements were collected over a range of incoming transonic Mach numbers for the middle-of-the-aperture elevation angle of 105 degrees. The National Instruments data acquisition system sampled 11 Kulite pressure sensors at the sampling rate of 54 kHz, which is 4 times of the wavefront sampling rate and was synchronized with the wavefront sensor.

In addition, a high-speed shadowgraph system was used to record the topology of the shock and the separated region on top of the cylinder turret in a range of transonic Mach numbers, see Figure 2. To do so, expanded and collimated laser beam 4-inch in diameter was transmitted into the test section in the spanwise direction using steering mirrors. The beam was passed through the test section and reflected back along the same path; the returning beam was split aside and re-imaged to a second high-speed video camera. The camera frame rate was 13.5 kHz, the same as the wavefront sensor sampling rate, with exposure time approximately 0.4 microseconds and the frame size of 640x640 pixels.

One of high-speed cameras was operating as the master one, supplying the frame synchronized clock signal to the slave camera; the master camera was also the source of triggering signal for the slave one and for the pressure acquisition system to synchronize shadowgraphs, wavefronts and pressure measurements.

### III. Data Reduction

For each collected wavefront sequence, wavefronts were computed using in-house software. After wavefront sequences were reconstructed, instantaneous tip/tilt and piston components from each wavefront within the sequence were removed. The time-average wavefront, that is a steady lensing, was also removed from each wavefront. As wavefronts were found to be almost spanwise uniform [16], wavefronts were averaged in the spanwise direction and were finally normalized as,

$$WF_{Norm}(\theta, t) = \frac{\langle WF(\theta, z, t) \rangle_{z-direction}}{\frac{\rho}{\rho_{SL}} M^2 D} \quad [\mu m / m],$$

where  $\rho$  is the free stream density,  $\rho_{SL}$  is the density at sea level,  $M$  is the Mach number at the port P1 at  $x/D = -0.625$  and  $D$  is the turret diameter.

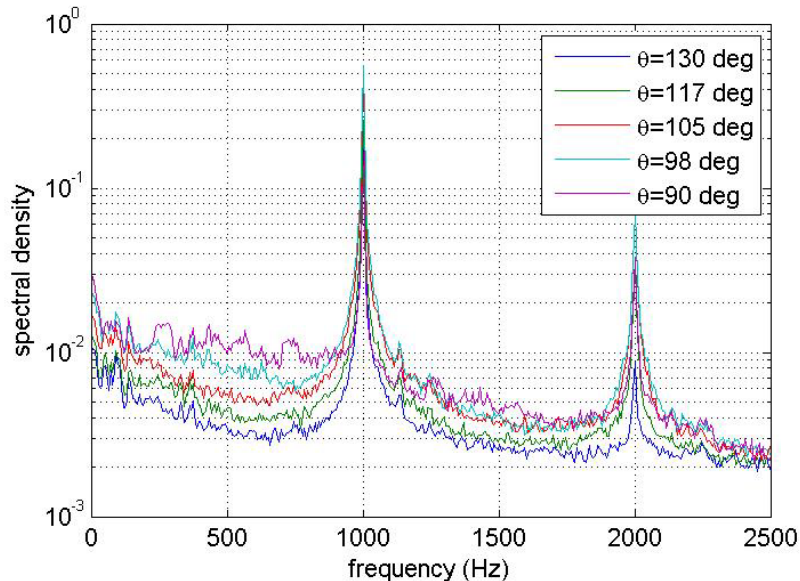


Figure 3. Spectra of unsteady pressures at selected locations over the aperture. Incoming  $M = 0.67$ .

To enhance the shadowgraph images, for every sequence an average image was computed over 2000 frames (approx. 150 periods) and it was subtracted from every image within the sequence.

As it will be shown later in this paper, most of the studied flow regimes, depending on the incoming flow speed, are unsteady. These regimes are characterized by the presence of strong periodic shock oscillations and the turret surface unsteady pressures and test section wall unsteady pressures at these regimes were found to have strong dominant frequency in their spectra. The example of spectra of fluctuating pressure at the turret surface is presented in Figure 3. A main harmonic of 1 kHz along with a second harmonic at 2 kHz are present in all spectra, implying a strong periodicity of flow features. Thus, a phase-locking averaging was implemented to analyze the flow dynamics and the characteristic features of the flow oscillations.

To perform the phase-locked averaging of pressure, the phase of the pressure signals had to be determined and corrected for low-frequency wandering. The phase detection was performed using reference sinusoid of the same frequency as the dominant oscillations. The signal of pressure and the reference signal were cross-correlated to determine a time delay and hence the phase difference between the signals. The cross-correlations were calculated using Blackman window, its width was chosen to fit 4-5 periods of dominant oscillations,  $T$ . The window was slid along the pressure signal with 50% overlapping, giving the phase delay at time moments with intervals of 2-2.5  $T$ . When the normalized cross-correlation between pressure and reference signals had no maximum above 0.1 it was assumed that no correlation can be found for those signals. These phase delays between signals of pressure and reference sinusoid were computed for every pressure sensor. Then the mean phase delay was calculated as an average over those signals, which phases were in the range of  $\pm 0.05 T$  from each other. Depending on the flow regime, those pressure signals were ranging from, in the worst case, four sensors on the turret at location from 94 to 105 degrees up to all nine unsteady pressure sensors. The mean phase was used to compute correction to phases of pressure signals when performing phase-locked averaging.

Once times were related to the phases using the above-described procedure, wavefronts were also assigned to particular phases and then ensemble-averaged to get phase-averaged wavefronts. A similar procedure was also initially applied to shadowgraph movies, but the ensemble-averaging procedure was found to smear many turbulent features. Finally, a single representative shadowgraph image was assigned to each phase.

In addition to visualizing the topology of the shock and the separated region, the shadowgraph images were used to determine the approximate location of separation line and the angle of the separation streamline on the turret at every phase.

#### IV. Results

A preliminary study of aero-optical environment around the 2-D turret was performed by Gordeyev et al. [16]. It was found that depending on the incoming speed, the flow had several regimes. At the incoming Mach number less than 0.6, the flow was found subsonic everywhere around the turret. When the incoming speed was increased above  $M = 0.63$ , the local supersonic flow region begins to appear near the top of the cylinder and the local shock was observed to form, stationary or unsteady depending on the Mach number, see Figure 4. The Mach number distributions along the test section for different flow regimes are shown in Figure 5. The flow regimes are assigned as “Case 1” – “Case 6” in the order of decreasing the outlet back pressure. As it can be seen from Figure 5, the flow reaches a maximum speed immediately past the turret top; also the flow becomes choked at flow regimes above Case 4, where the incoming speed did not change with the further decrease of the outlet back pressure, the flow over and downstream of the turret was continuously increasing and becoming supersonic shortly downstream of the turret. To differentiate the cases, the local Mach number at the static pressure port P6 at  $x/D = 0.625$  was chosen. Local Mach numbers at locations P1,  $x/D = -0.625$ , and P6,  $x/D = 0.625$ , see Figure 1, left, for all studied cases are given in Table 1.

The mean pressure distributions over the aperture, normalized by the incoming total pressure, for different cases are shown in Figure 6, left. As the flow speed over the turret increases, the mean pressure at the turret initially decreases, indicating the flow acceleration on the top of the turret, as the curved cylinder surface worked as a convergent-divergent nozzle. At some point the flow becomes supersonic at the upstream portion of the aperture, as the normalized local pressures were below 0.52 (an isentropic pressure ratio, corresponding to a sonic Mach number). The pressure reaches the minimum value between elevation angles 95 and 100 degrees, followed by the sharp increase, which is related to the time-averaged presence of the shock. By the end of the aperture, pressure approaches a constant value, indicating the flow separation region downstream of the shock. This spatial pressure distribution is observed for all cases, except for the Case 3, where the mean pressure over the aperture shows a monotonic increase over the aperture; as it will be discussed later, the range of the shock motion was the largest for this case. For Cases 4-6 the all normalized pressures are below 0.52, implying that the flow is supersonic over the

aperture. The fluctuation pressure distributions, normalized by the incoming total pressure are presented in Figure 6, right. The unsteady pressure field has a maximum fluctuation level between 95 and 100 degrees, indicating the location of the unsteady shock, with Cases 3 and 4 having the strongest fluctuation levels, compared to other cases.

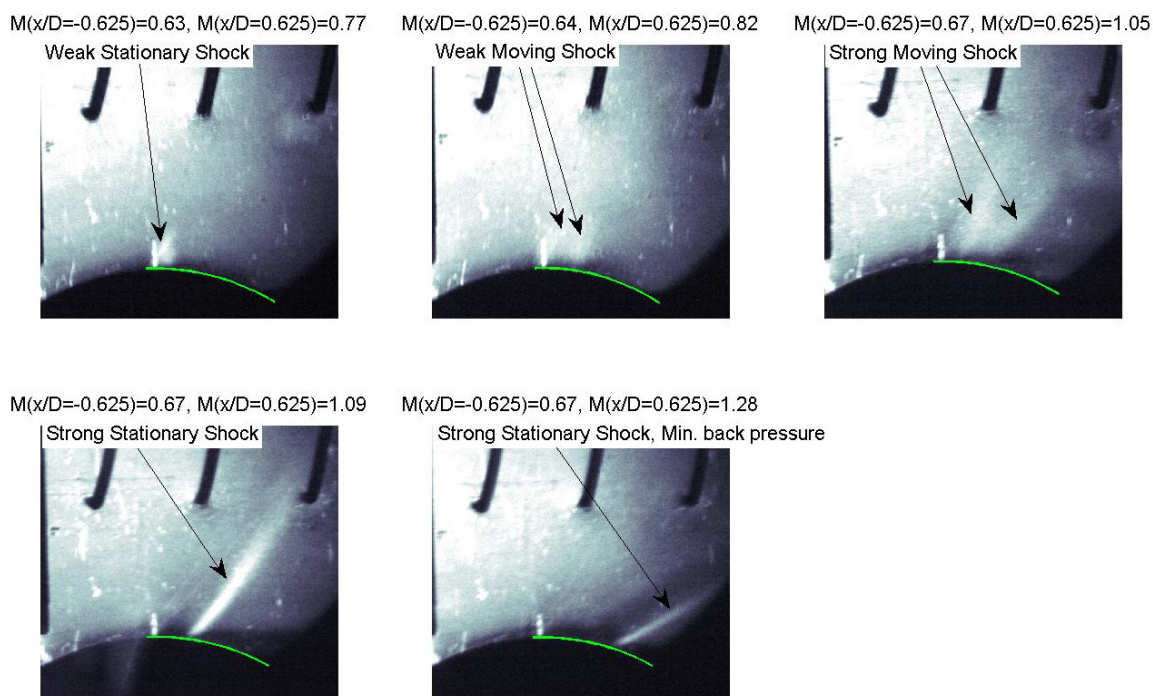


Figure 4. Long-exposure schlieren flow visualization for different flow regimes. From [16].

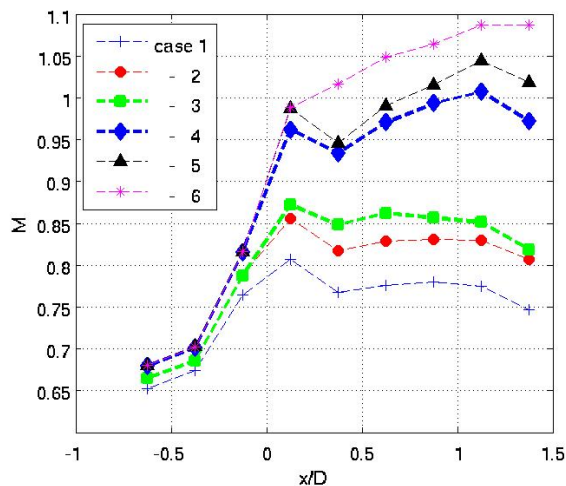


Figure 5. Distribution of Mach number along the test section at different flow regimes.

Table 1. Mach numbers at locations  $x/D=-0.625$  and  $x/D=0.625$  for all studied cases.

Case	Case 1	Case 2	Case 3	Case 4	Case 5	Case 6
$M(x/D=-0.625)$	0.6528	0.665	0.665	0.6794	0.6805	0.6805
$M(x/D=0.625)$	0.7754	0.8284	0.8621	0.9706	0.991	1.0488

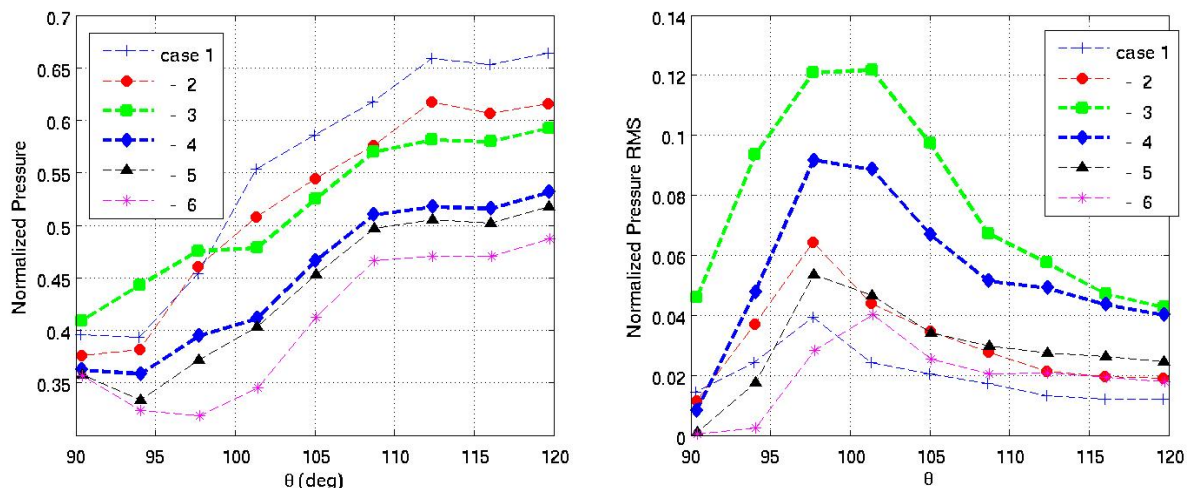


Figure 6. Normalized mean (left) and fluctuating (right) pressures on the turret at different flow regimes.

Unsteady pressure spectra at the surface location of  $\theta = 98$  degrees, where the pressure fluctuations were found to be the largest, are shown in Figure 7 for all six cases. For Case 1 the local pressure fluctuation was the weakest among all cases, with the main frequency around 1 kHz, and with the evidence of a subharmonic near 500 Hz. The subharmonic has a broad peak, suggesting pseudo-periodic motion of the shock for Case 1; this observation was confirmed by analyzing time-resolved shadowgraphs. Case 2 has a similar spectrum as Case 1, but with the presence of additional higher harmonics. Cases 3-6 do not have the subharmonic and only have the main mode and higher harmonics in their spectra. The peak frequency of the main mode monotonically shifts from 1040 Hz for Case 1 to 930 Hz for Case 6. This frequency dependence of the local Mach number will be further investigated in Section V, where a low-dimensional model of the shock-separation interaction will be presented.

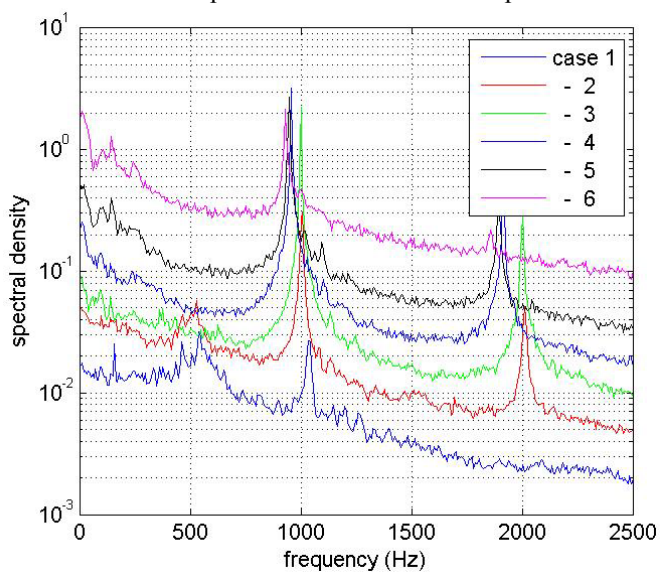
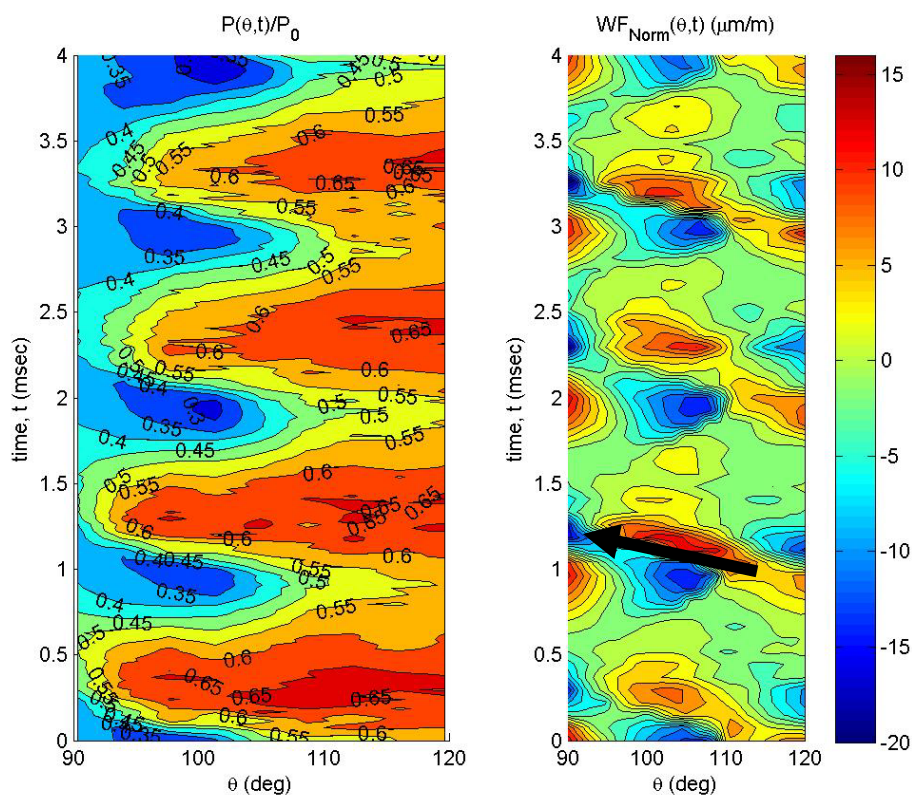


Figure 7. Temporal pressure spectral densities for all cases at  $\theta = 98$  degrees. Spectra plots were shifted for clarity.

Detailed analysis of the pressure variation and the shadowgraph movies revealed that for Case 1 the presence of the subharmonic, combined with the relatively-weak main harmonic, made the determination of the phase and other flow features, like the separation streamline angle, difficult, and no phase-averaging can be done, but qualitatively Case 1 was found to be similar to Case 2. Also, Cases 5 and 6, and to some degree, Case 2 were found to be similar to Case 4. So, to present dynamics of the shock and the separated region, only Cases 3 and 4 will be discussed in this paper.

An example of temporal-spatial evolution of the unsteady surface pressure and related simultaneous spanwise-averaged wavefronts for Case 3 is presented in Figure 8. Periodic variation in the surface pressure and related periodic variation in wavefronts is evident. A sharp discontinuity in the wavefront slices, marked by a large arrow in Figure 8, right, is indicative of the unsteady shock present over the aperture. The shock exhibits primarily upstream motion. A typical non-dimensional frequency of the shock motion, based on the incoming speed and the turret diameter was found to be between 0.5 for Case 1 and 0.42 for Case 6. A very similar shock dynamics, including the upstream shock motion and similar oscillation frequencies, was observed over hemispheric turrets at transonic speeds in flight [5].



**Figure 8. Simultaneous time-dependent surface pressure distribution (left) and spanwise-averaged wavefronts (right). Case 3,  $M(x/D = 0.625) = 0.86$ . The shock is labeled as a thick black arrow in the left plot.**

Figure 9 shows selected shadowgraphs for Case 3, where the temporal evolution of the flow is presented during eight characteristic phases. The phase-locked average of the normalized pressure along the aperture and spanwise-averaged wavefront at the same phase are plotted at the upper left corner of every image; the dashed line represent the isentropic normalized pressure corresponding to  $M = 1$ . During phase = 0 degrees, the shock is at its maximum strength and the separation streamline angle, later called the separation angle, is large. The wavefront plot indicates the presence of significant disturbances created by the shock, but because of the oblique nature of the shock the wavefront does not show a shock-related discontinuity. By the phase = 90 degrees, the shock reaches its most upstream location, and its strength decreases significantly; the separation angle is still relatively large. Starting this moment the adverse pressure gradient is not strong enough to force the flow separation immediately downstream of the shock, so the separation region no longer forms immediately downstream of the shock and the separation point moves downstream, while the shock keeps decreasing in strength, as seen for phase = 150 degrees; the spatial variation of the wavefront also keeps decreasing. During phase = 210 degrees, the shock is essentially gone, which agrees with aero-optical measurements as the wavefront variation is at its minimum. The separation point moves downstream to approximately 105 degrees; the pressure over the entire aperture keeps decreasing at this phase. At the phase = 240 degrees, aero-optical disturbances get stronger with the local sharp increase in the middle of the aperture, as the shock starts forming there. The similar behavior is also observed for phase = 270 degrees, where the small local normal shock is visible in the shadowgraph image and the sharp increase in the wavefront gets larger. At phase = 300 degrees, the shock grows longer into the freestream flow and the separation angle starts increasing, as

the stronger shock promotes a stronger gradient across it and forcing a larger separation. During phase = 330 degrees, the shock is near its maximum strength and the separation angle is the largest. The large separation region starts blocking the flow downstream of the shock, thus pushing it forward, as seen for phase = 0 degrees, thus competing the cycle.

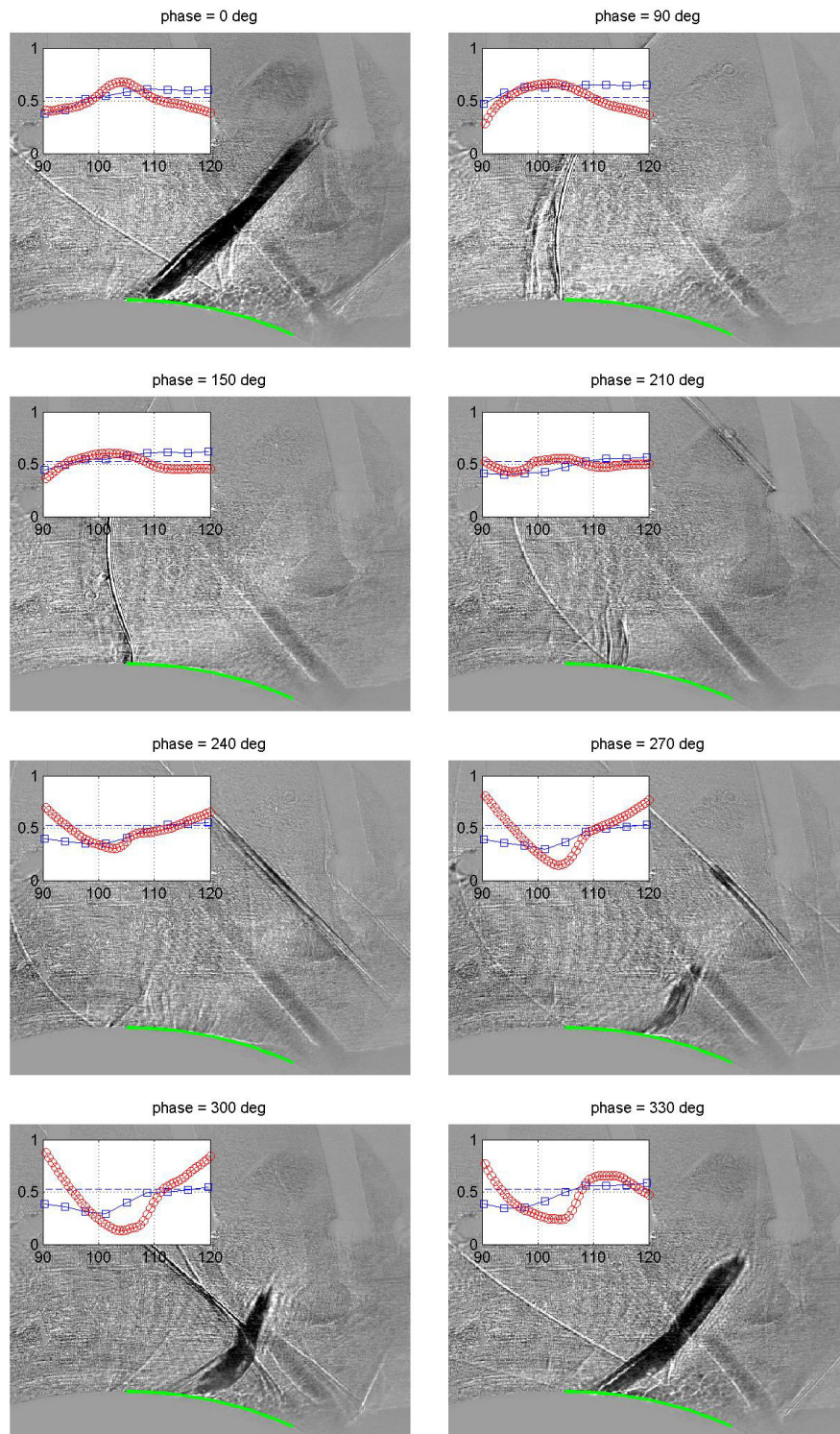


**Figure 9. Shock temporal evolution, along with pressure distribution and spanwise-averaged wavefront presented in upper left insert, for Case 3 at selected phases.  $M(x/D = 0.625) = 0.86$ . Green line represents the location of the aperture.**

In summary, the interaction between the shock and the shock-induced flow separation leads to an increase of flow blockage, which results in the upstream shock motion. When the shock is pushed upstream, it gets weaker and the separation region gets smaller, lessening the flow blockage downstream. The shock re-forms downstream, eventually increasing its strength and resulting in the increased flow separation and blockage, thus completing the cycle. A similar shock-separation interaction, resulted in low-frequency shock oscillations was observed in the shock-induced separation on the wall of a slightly-overexpanded supersonic nozzle [23].

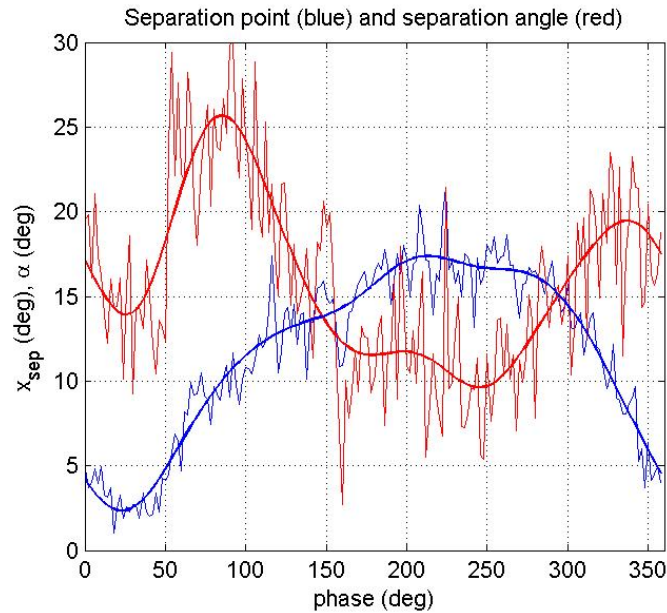


**Figure 10. Angular coordinate of separation point,  $x_{sep}$ , (blue) and the angle of separated streamline,  $\alpha$ , (red) for Case 3.  $M(x/D = 0.625) = 0.86$ . Thicker lines correspond to low-pass-filtered results.**

Using shadowgraph images, the separation location,  $x_{sep}$ , measured as an angle from the top of the turret (which correspond to  $\theta = 90$  degrees), and the separation angle,  $\alpha$ , were extracted as a function of phase and results are shown in Figure 10 as thin lines. A low-pass filter was applied to smooth out the inherent noise in the data and the results are also plotted in Figure 10 as thicker lines. As described before, starting at phase = 30 degrees, the separation point, located at 3 degrees away from the turret top, starts moving downstream, with the increasing separation angle. The separation angle reaches a maximum value of 25 degrees for phase = 90 degrees and then quickly dropping to 10 degrees by phase = 150 degrees. By phase = 250 the shock starts forming at 17 degrees downstream of the turret top, getting stronger by phase = 300 degrees, and forcing the increase of the separation angle from 10 to 20 degrees; the separation location is unchanged within this phase range. Starting at phase 300 degrees, the shock moves upstream, forcing the separation point to move upstream as well.

The shock-related dynamics in Case 3 exhibits strong asymmetry vs phase, which is evident by comparing the shock motion during the upstream and the downstream motion in Figures 9 and 10. During the upward shock motion, which corresponds to phase range from 270 to 90 degrees, the shock is clearly visible, while during the downstream motion, corresponding to phase range between 90 and 270 degrees, the shock is virtually not present. During the upstream stroke, separation line initially follows the shock, but eventually gets detached from it and goes back to the location of  $\theta = 105$  degrees. The similar asymmetry in the shock dynamics was observed around turrets in flight [5].

Another way to see this asymmetry is presented in Figure 11, left, where the phase-averaged pressures are plotted as a function of phase and the angular location on the aperture. Separation locations for different phases are plotted as open circles in both plots. The shock location can be identified where the pressure has sharpest positive gradient, or, equivalently, where the contour lines are the closest. The separation point follows the shock between phases 0 and 50 degrees and then between phases 250 and 360 degrees, while the shock and the separated point are clearly different for phases between 50 and 250 degrees. A similar conclusion can be reached analyzing the phase-averaged wavefronts presented in Figure 11, right; the separation points are also indicated by open circles. As the shock creates the sharp positive gradient in the wavefront, the shock location was identified, where the maximum

wavefront gradient in the streamwise direction is larger than a prescribed threshold; these locations for different phases are marked as black filled diamonds in Figure 11, right. Again, the separation line forms immediately after the shock only in phase ranges between 0 and 50 degrees and 250 and 360 degrees. In fact, the shock is not detected during phases between 50 and 250 degrees, consistent with shadowgraph images in Figure 9.

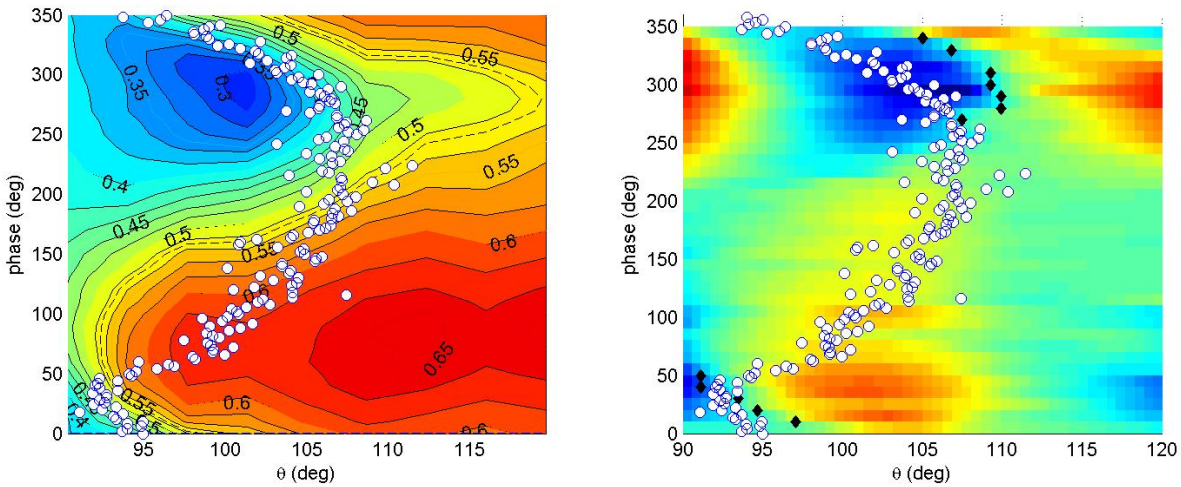


**Figure 11. Spatial variation of phase-avegared surface pressure distribution (left) and spanwise-averaged wavefronts (right). Separation locations are marked by open circles in both plots. Case 3,  $M(x/D = 0.625) = 0.86$ .**

Shadowgraph images, pressure and wavefront spatial distributions during selected phases for Case 4 are shown in Figure 12. These are the same phase angles as for Case 3, presented in Figure 9. The shock-separation dynamics for Case 4 is similar to the one for Case 3, with few differences. One difference is that the shock in Case 4 is overall stronger, the separation angles are more pronounced and aero-optical wavefronts are stronger. Also, unlike Case 3, the separation point is always formed immediately downstream of the shock. During the downstroke the shock is present, but is weak, compared to the shock upstroke. Finally, the asymmetry in the shock upstream and downstream motion and intensity, while still observable, gets weaker for Case 4.

The separation location and the separation angle for Case 4 for different phases are presented in Figure 13. The separation point moves between 5 and 15 degrees away from the top of the turret and the separation angle varies between 10 and 20 degrees. Similar to Case 3, the separation angle increases between phases 250 and 50 degrees, while the shock location is mostly unchanged; this phase range corresponds to the shock penetrating farther into the freestream flow, as seen in Figure 12. Between phases 50 and 150 degrees, the shock retreats forward and weakens, so the separation angle decreases in this phase range.

The phase – spatial-distribution maps of the pressures and wavefronts for Case 4 are presented in Figure 14, left and right plots, respectively, along with the separation locations marked as open circles. As mentioned before, the separation point is always immediately downstream of the shock, see Figure 14, left. The shock presence was computed from wavefronts using the threshold criterion and locations at different phases are marked by black diamonds. As the shock is oblique for most phases, the largest gradient is not necessarily indicative of the shock presence. For instance, the shock is present for phases 0 and 90 in Figure 12, but does not create a large gradient in the wavefront.

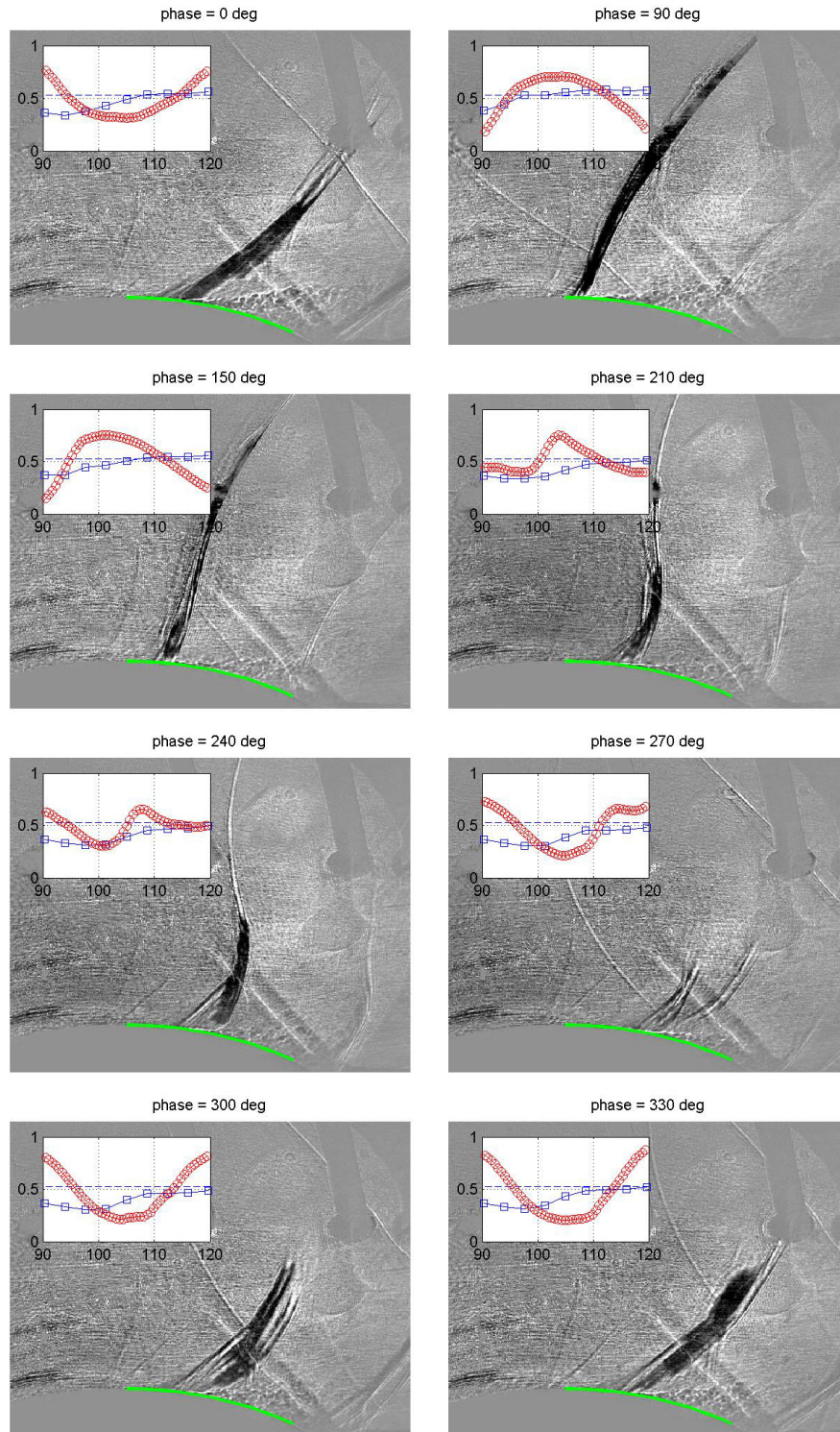
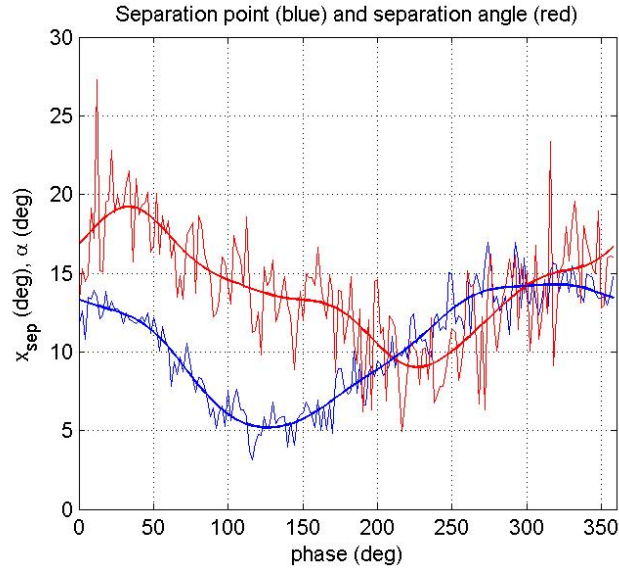
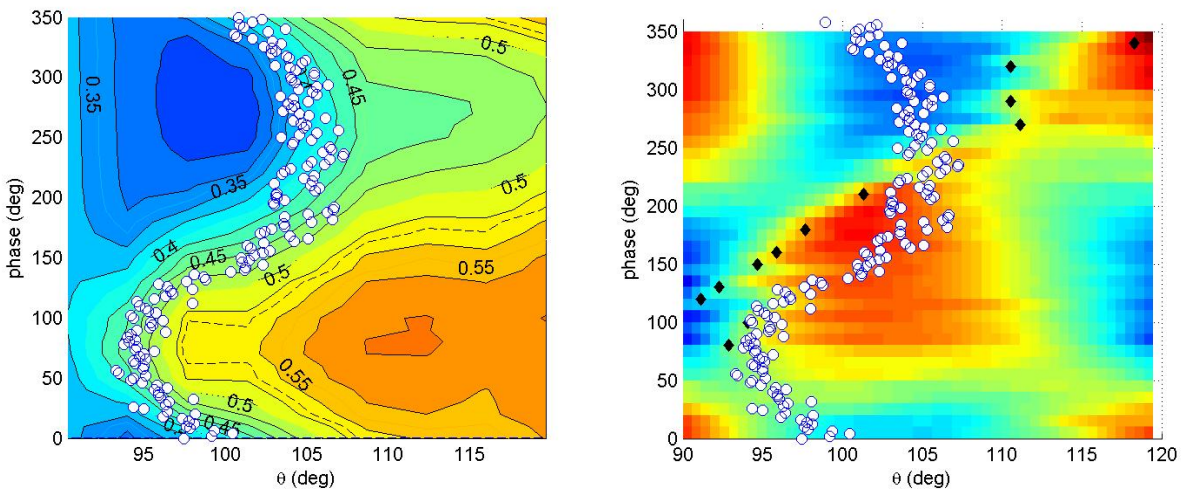


Figure 12. Shock temporal evolution, along with pressure distribution and spanwise-averaged wavefront presented in upper left insert, for Case 4 at selected phases.  $M(x/D = 0.625) = 0.97$ . Green line represents the location of the aperture.



**Figure 13. Angular coordinate of separation point,  $x_{sep}$ , (blue) and the angle of separated streamline,  $\alpha$  (red) for Case 4.  $M(x/D = 0.625) = 0.97$ . Thicker lines correspond to low-pass-filtered results.**



**Figure 14. Spatial variation of phase-averaged surface pressure distribution (left) and spanwise-averaged wavefronts (right). Separation locations are marked by open circles in both plots. Case 4,  $M(x/D = 0.625) = 0.97$ .**

Presented results clearly indicate that there is strong coupling between the shock location and strength and the separated region location and size, as the shock modifies the downstream pressure field to affect the separation region, resulting in changes in the downstream pressure, which affects the shock. In the next section a low-dimensional model will be proposed in attempt to explain key unsteady features of the shock-separation interaction.

## V. Low-Dimensional Model of the Shock-Separation Interaction

Relatively low frequencies of the shock-separation motion, about 0.5, based on the turret diameter, and the periodic nature of the interaction, rules out the incoming boundary layer as a main reason of this temporal evolution. Inspired by a physical mechanism of the shock-separation interaction in over-expanded nozzle proposed in [23], we have attempted to develop a low-dimensional model of the shock-separation interaction around the cylindrical turret. Figure 15 presents a model schematic of the flow downstream of the shock and defined several parameters. The instantaneous separation point is denoted by  $x_{sep}$ , the angle between the turret surface and the separated streamline is denoted by  $\alpha(t)$ . Pressure in the separation region downstream of the separation point is denoted by  $P_s(t)$ , the exit

pressure,  $P_E$ , is considered to be constant. The u-component of the velocity in the separation region is assumed to be positive toward upstream direction. Once the separation region is defined by  $x_{sep}$  and  $\alpha$ , and the exit pressure is given, the shock location and shock angle can be calculated.

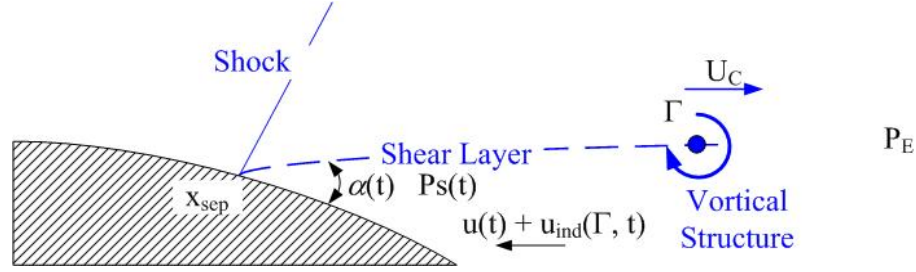


**Figure 15. Schematic of the shock-separation topology and definition of parameters used in modeling.**

The momentum equation in the simplified form describes the changes in the u-velocity due to the pressure gradient along the separation region,

$$\frac{du(t)}{dt} \sim \frac{dp}{dx} \sim -(P_S(t) - P_E) \quad (1a)$$

From the conservation of mass, the influx of u-velocity increases the separation pressure,

$$\frac{dP_S(t)}{dt} \sim \frac{d\rho_S(t)}{dt} \sim (u(t) + u_{ind}(t)) \quad (1b)$$

Also, the velocity influx will move the separation line upward, increasing the separation angle,

$$\frac{d\alpha(t)}{dt} \sim (u(t) + u_{ind}(t)) \quad (1c)$$

Changes of the separation angle leads to vorticity generation at the separation point,

$$\frac{D\omega(x,t)}{Dt} = \frac{\partial\omega(x,t)}{\partial t} + U_C \frac{\partial\omega(x,t)}{\partial x} \sim \frac{d\alpha(t)}{dt} \quad (1d)$$

The vorticity will create induced u-velocity, but at a retarded time. In a simplified form,

$$u_{ind}(t) \sim \int_{x_{sep}}^{\infty} \frac{\omega(x - x_{sep}, t - (x - x_{sep})/a) \cdot A(x - x_{sep})}{x - x_{sep}} dx \quad (1e)$$

is the retarded induced velocity due to the vortical structure formed at  $x - x_{sep}$  downstream of the separation point.  $a_0$  and  $U_C$  are the speed of sound in the separated region and the convective speed of the vortical structure, respectively, and  $A(x)$  is the modulation function, describing the structure “formation”.

From (1a) and (1b) it follows,  $\frac{d^2 P_S(t)}{dt^2} \sim \frac{du(t)}{dt} + \frac{du_{ind}(t)}{dt} \sim -(P_S(t) - P_E) + \frac{du_{ind}(t)}{dt}$ , or,

$$\frac{d^2 P_S(t)}{dt^2} + \Omega^2 (P_S(t) - P_E) \sim \frac{du_{ind}(t)}{dt} \quad (2)$$

which corresponds to harmonic oscillations with the forcing term due to the retarded induced velocity.

Comparing (1b) and (1c) leads to  $\frac{d\alpha(t)}{dt} \sim \frac{dP_S(t)}{dt}$ , saying that the pressure in the separation region is in phase with the separation angle.

From (1d) it follows that  $\omega(x,t) \sim \alpha(x - U_C t) \sim P_S(x - U_C t)$ , which implies that the generated vorticity at downstream location,  $x - x_{sep}$ , is proportional to the separation pressure at an earlier retarded time  $t - (x - x_{sep})/U_C$ .

We assume that the induced velocity is only from the nearest vortical structure which forms starting at some distance,  $L$ , away from the separation point at the location of the maximum vorticity with the intensity,  $\Gamma$ , proportional to the maximum vorticity,

$$\omega(x, t) \sim \Gamma \cdot A(x - x_{sep}) \cdot \delta(x - U_c t),$$

where  $\delta$  is the delta-function and the A-function is schematically drawn in Figure 16. Let's say the separation pressure reaches a maximum at some moment in time. In approximately  $L/U_c$ -time later the structure is formed at the location  $L$  and in even later  $(L/U_c + L/a_0)$ -time the induced velocity from the structure reaches the separation point upstream. In order for the delayed forcing term to create a resonance, it should be in phase with the separation pressure,

$$(L/U_c + L/a_0) = n/F, \quad (3)$$

where  $F$  is the resonance frequency and  $n$  is an integer number. This equation is essentially the Rossiter-type resonance equation, but  $L$  is not necessarily a constant and might be a function of the convective speed of the vortical structure. Let's assume that  $L = U_c \tau$ , where  $\tau$  is a characteristic time it takes for the structure to form. The convective speed for the shear-layer structure is  $U_c = 0.5U_\infty = 0.5Ma = 0.5Ma_0 / \sqrt{1 + 0.2M^2}$ , where  $a$  is the speed of sound in the freestream above the separation region. Substituting both of the above equations into (3) and solving for  $F$  gives the following equation for the resonance frequency,

$$F = \frac{n}{\tau} \left( 1 + \frac{0.5M}{\sqrt{1 + 0.2M^2}} \right)^{-1} \quad (4)$$

This equation describes a resonance frequency dependence on the Mach number in the freestream above the separated region. From Figure 7 frequencies of the main harmonic were extracted for all cases and the local Mach number at  $x/D=1.125$  was chosen as a freestream Mach number. Results are plotted in Figure 17 as squares. The model (4) with  $n=1$  has only one empirical constant,  $\tau$ . This time scale can be treated as a typical time scale to form the compact vortical structure in the moving frame of reference. By trial and error, the best fit between the experimentally-observed and predicted frequencies was found for  $\tau = 0.715$  msec and the resulted predicted frequencies are also plotted in Figure 17 as a solid line; the agreement was found to be good. The model even predicts the frequency of shock oscillations for Case 1, where no strong periodic shock motion was found.

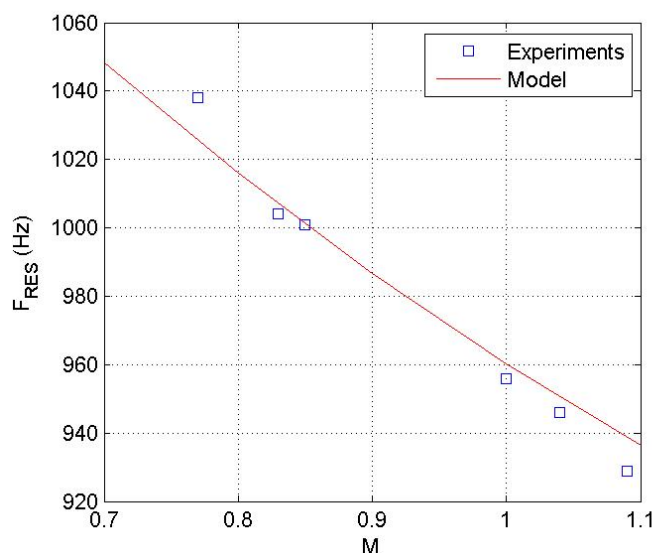


**Figure 17. Experimentally-observed frequencies vs freestream Mach number, compared with the model prediction, (4), for  $n = 1$ ,  $\tau = 0.715$  msec.**

From the model it follows that the separation pressure and the separation angle should be in phase. The separation pressure at the elevation angle of 112 degrees and the separation angle for different phases are presented in Figure 18 for Case 3 and Case 4. Indeed, the separation pressure and the separation angle are approximately in phase for both cases.

While the shock is not directly present in the model, the shock is responsible for the formation of the separation region with the well-defined separation point and the separation angle, which was assumed in the model.

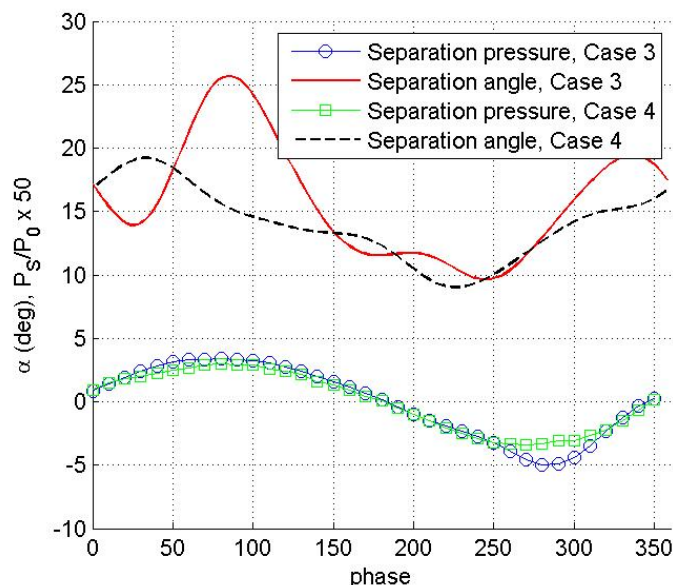


**Figure 18. Phase dependence of the separation normalized pressure at  $\theta = 118$  degrees (mean removed and multiplied by a factor of 50 for clarity) and the separation angle for Cases 3 and 4.**

Of course, the presented model is too simplistic to address all features of the complex shock-separation interaction or to predict details of temporal variation in the surface pressures or wavefront distortions. For instance, it does not address why the resonance peak in most cases is so sharp, which is most probably a consequence of the non-linear effects due to large oscillations of the pressure field and the tunnel-wall blockage. Rather, it should be treated as a plausible explanation of the physical mechanism responsible for starting and sustaining the resonance, which gives the right trends and identifies probable sources of flow instabilities.

## VI. Conclusions and Discussion

Time-resolved measurements of aero-optical aberrations of the flow around a two-dimensional cylindrical turret, simultaneously with flow visualization with high-speed shadowgraph system and unsteady pressure measurements on the surface of the turret were performed and documented at different transonic flow regimes. It was found that the flow exhibits self-sustained oscillatory behavior above a critical incoming Mach number, when the unsteady local shock is formed on top of the turret. The amplitude of the shock-related flow oscillations as well as the dynamics of the shock and the separation region were found to be dependent on the incoming flow velocity. It was found that the frequency of flow oscillations decreases as the flow velocity increases. Based on the unsteady pressure signal near the shock, the phase-averaging procedure was used to extract shadowgraphs, wavefronts and surface pressures at different phases. The locations of the shock and separation were determined from high-speed shadowgraphs to analyze the shock topology and to correlate it with aero-optical distortions created by the compressible flow. The self-sustained oscillations were the result of the strong shock-separation interaction, as the shock in the farthest downstream location creates a strong separation region, which blocks the flow downstream of the shock and pushes the shock upstream. When the shock goes upstream, it loses its intensity and the separation region becomes smaller. It results in the shock re-formation farther downstream, thus completing the cycle. In some cases the separation point was found to be detached from the shock. Asymmetry between the upstream and the downstream motion of the shock was found in most cases, where the shock and the separation region topology during the upstream motion were different from the topology during the downstream motion, as the shock was stronger during the upstream motion. Based on observation of temporal dynamic of the shock-separation dynamics, a low-dimensional model, based on the time-delayed feedback mechanism, was proposed to explain the existence of the resonance. The derived model satisfactorily explained the frequency dependence versus the local Mach number, as well as some other essential features of the shock-separation interaction.

The proposed low-dimensional model addresses possible sources of the low-frequency oscillations of the shock, observed around turrets in flight. It identifies a global feedback mechanism, where the shock creates distortions in the separation region, which convect with the separated flow and eventually complete the feedback via acoustical radiation. Other word, the low-frequency oscillations of the local shock at transonic speeds are most probably due to resonant modes excited in the separation region. For three-dimensional turret, the resonance feedback is weakened by three-dimensional and turbulent nature of the separated region, inevitably smearing out and reducing the resonance peak. Nevertheless, the presence of the vertical “breathing” mode experimentally observed in the separated region downstream of the hemisphere-on-cylinder turret at subsonic speeds at a relative-low normalized frequency range of  $St_D = fD/U_{inf} = 0.3..0.5$  [24], which is similar to normalized frequencies observed in this experiment, also can be explained with the existence of weak resonance in the separated region around realistic turrets. While this frequency range was observed at subsonic speeds, the presence of the local shock at transonic speeds might enhance this resonance feedback mechanism.

### Acknowledgements

This work was funded by the Air Force Research Laboratory, Directed Energy Directorate. The U.S. Government is authorized to reproduce and distribute reprints for governmental purposes notwithstanding any copyright notation thereon.

### References

- [1] S. Gordeyev and E. Jumper, “Fluid Dynamics and Aero-Optics of Turrets”, *Progress in Aerospace Sciences*, **46**, (2010), pp. 388-400.
- [2] Gilbert, K. G. and Otten L. J. (eds), “Aero-Optical Phenomena,” *Progress in Astronautics and Aeronautics*, Vol. 80, AIAA, New York, 1982.
- [3] M. Wang, A. Mani and S. Gordeyev, ”Physics and Computation of Aero-Optics”, *Annual Review of Fluid Mechanics*, Vol. **44**, pp. 299-321, 2012.
- [4] C. Porter, S. Gordeyev, M. Zenk and E. Jumper, "Flight Measurements of the Aero-Optical Environment around a Flat-Windowed Turret", *AIAA Journal*, Vol. **51**, No. 6, Jun. 2013, pp. 1394-1403.
- [5] N. De Lucca, S. Gordeyev and E.J. Jumper, "In-flight aero-optics of turrets", *Journal of Optical Engineering*, **52**(7), 071405, 2013.
- [6] B. Vukasinovic, A. Glezer, S.Gordeyev, E. Jumper and V. Kibens, "Hybrid Control of a Turret Wake," *AIAA Journal*, Vol. **49**, No. 6, pp. 1240-1255, 2011.
- [7] M. Palaviccini, L. Cattafesta and B. George, ”Passive Flow Control over a Three-Dimensional Turret with a Flat Aperture”, AIAA Paper 2011-3265, 2011.
- [8] B. Vukasinovic, A. Glezer, S. Gordeyev, E. Jumper and V. Kibens, "Active Control and Optical Diagnostics of the Flow over a Hemispherical Turret”, AIAA Paper 2008-0598, 2008.
- [9] B.H.K. Lee, ”Self-sustained shock oscillations on airfoils at transonic speeds”, *Progress in Aerospace Sciences*, **37**, pp. 147-196, 2001.
- [10] D.S. Dolling, ”Fifty years of shock-wave/boundary-layer interaction research: what next?”, *AIAA Journal*, **39**(8), pp.1517–1531, 2001.
- [11] Green J.E. “Interaction between shock waves and boundary layers” *Progress in Aerospace Sciences*, **11**, pp. 235-340, 1970.
- [12] Delery J.M. “Shock wave/turbulent boundary layer interaction and control”, *Prog. Aerospace Sci.*, **22**, pp. 209-280, 1985.
- [13] Smits A.J., Dussauge J.P. *Turbulent shear layers in supersonic flow*, 2nd Edition, American Institute of Physics, NY, 2005.
- [14] Andreopoulos Y, Agui JH, Briassulis G. Shock Waves-Turbulence Interactions. *Annual Review of Fluid Mechanics*, **32**, pp. 309-345, 2000.
- [15] Benard, E., Huang, J.-C. and Raghunathan, S. *Experimental investigation of unsteadiness in transonic shock boundary layer interaction*. In: 45th AAAF Symposium of Applied Aerodynamics, 22-24 March 2010, Marseille, France.
- [16] Gordeyev, S., Burns, R., Jumper, E.J., Gogineni, S., and Wittich, D.J., “Aero-Optical Mitigation of Shocks Around Turrets at Transonic Speeds Using Passive Flow Control,” AIAA Paper 2013-0717, 2013.
- [17] B. Vukasinovic, A. Gissen, A. Glezer and S. Gogineni, ”Fluidic Control of Transonic Shock-Induced Separation”, AIAA Paper 2013-0529, 2013.

- [18] R. Burns, S. Gordeyev, E. Jumper, S. Gogineni, M. Paul and D.J. Wittich, “ Estimation of Aero-Optical Wavefronts Using Optical and Non-Optical Measurements ”, AIAA Paper 2014-0319., 2014.
- [19] S. Gordeyev, J.A. Cress, E. Jumper and A.B. Cain, "Aero-Optical Environment Around a Cylindrical Turret with a Flat Window", *AIAA Journal*, Vol. 49, No. 2, pp. 308-315, 2011.
- [20] S. Gordeyev, E. Jumper, T. Ng and A. Cain, "The Optical Environment of a Cylindrical Turret with a Flat Window and the Impact of Passive Control Devices", AIAA Paper 2005-4657, 2005.
- [21] S.Gordeyev, J. Cress, A. Smith and E. Jumper "Improvement in Optical Environment over Turrets with Flat Window Using Passive Flow Control", AIAA Paper 2010-4492, 2011.
- [22] K. Wang, M. Wang, S. Gordeyev and E. Jumper, "Computation of Aero-Optical Distortions over a Cylindrical Turret with Passive Flow Control", AIAA Paper 2010-4498, 2010.
- [23] B.J. Olson and S.K. Lele,"Large-Eddy Simulation of an over-expanded planar nozzle", AIAA Paper 2011-3908, 2011.
- [24] N. De Lucca, S. Gordeyev and E. Jumper, “ Effect of Surface Unsteady Pressure Field on Global Beam Jitter for a Hemisphere-on-Cylinder Turret, ” AIAA Paper 2014-0322, 2014.